

Materials Advances

Accepted Manuscript

This article can be cited before page numbers have been issued, to do this please use: S. Tahira, S. Siddiqua, F. P. Malik and H. Rafique, *Mater. Adv.*, 2026, DOI: 10.1039/D5MA01336D.



This is an Accepted Manuscript, which has been through the Royal Society of Chemistry peer review process and has been accepted for publication.

Accepted Manuscripts are published online shortly after acceptance, before technical editing, formatting and proof reading. Using this free service, authors can make their results available to the community, in citable form, before we publish the edited article. We will replace this Accepted Manuscript with the edited and formatted Advance Article as soon as it is available.

You can find more information about Accepted Manuscripts in the [Information for Authors](#).

Please note that technical editing may introduce minor changes to the text and/or graphics, which may alter content. The journal's standard [Terms & Conditions](#) and the [Ethical guidelines](#) still apply. In no event shall the Royal Society of Chemistry be held responsible for any errors or omissions in this Accepted Manuscript or any consequences arising from the use of any information it contains.

DFT-Driven Insights into the Electronic, Magnetic, and Transport Properties of 2D Nb₃C₂ MXene for High-Performance Li-Ion Batteries

Samia Tahira^a, Safwara Siddiqua^a, Fouzia Perveen Malik^{a,}, Hummera Rafique^b*

^aMaterials Modelling Lab, School of Interdisciplinary Engineering & Science (SINES), National University of Sciences and Technology (NUST), H-12, Islamabad, 44000, Pakistan.

^bDepartment of Chemistry, University of Gujrat, Gujrat-50700, Pakistan



Corresponding Author

Fouzia Perveen Malik

Professor

School of Interdisciplinary Engineering & Science (SINES), National University of Sciences and Technology (NUST), Sector H-12, 44000 Islamabad, Pakistan.

Email: fouzia@sines.nust.edu.pk

Abstract

The two-dimensional material 'MXene' has attained significant attention for its outstanding characteristics inherent to nanostructures. However, to date, Nb₃C₂ MXene, particularly in Cr-doped form, has not been theoretically explored for Li-ion battery applications. In this work, first-principles calculations were performed to explore the structural, electronic, magnetic, and transport properties of newly designed pristine Nb₃C₂ and Cr-doped Nb₃C₂ along with their energy storage potential, using the FP-LAPW approach. Both structures are dynamically and thermally stable, as confirmed from phonon dispersion and AIMD simulations. Electronic properties, including band structure and density of states, indicate metallic behavior in both structures with an indirect band gap, fulfilling a key requirement for electrode materials in energy storage systems. Pristine Nb₃C₂ exhibits an essentially non-magnetic ground state, while Cr-doped Nb₃C₂ reveals ferromagnetic behavior. Theoretical capacities of 169 mAh g⁻¹ for pristine Nb₃C₂ and 280 mAh g⁻¹ for Cr-doped Nb₃C₂ were obtained, indicating a substantial enhancement upon Cr doping and exceeding that of pristine Nb₂C (170 mAh g⁻¹) reported in the literature. The predicted electrochemical properties unveil that both pristine and Cr-doped Nb₃C₂ possess favorable open-circuit voltages within the desirable range for anode materials, along with high electronic conductivity and improved gravimetric capacity. Furthermore, transport property analysis based on semi-classical Boltzmann theory highlights their promising thermoelectric behavior, complementing their electrochemical performance and providing a comprehensive evaluation of MXene in energy storage devices.

KEYWORDS: Cr-doped Nb₃C₂ MXene, Li-ion batteries, Ferromagnetism, Spintronics, Energy storage



1. Introduction

The successful synthesis and research on graphene have compelled scientists to explore more graphene-like 2D materials, both experimentally and theoretically, made of elements beyond carbon, such as phosphorene, hexagonal boron nitride (h-BN), and transition metal dichalcogenides. These materials possess unique properties, such as a high surface area-to-volume ratio and excellent electrical and thermal conductivity, making them promising candidates for use in supercapacitors and batteries [1].

However, the performance of current batteries is insufficient to adequately satisfy the escalating demand for extensive energy storage. In order to address and comprehend this challenge, an immediate imperative arises to actively pursue novel materials that exhibit enhanced performance attributes within energy storage systems [2]. Recently, a new class of 2D material known as MXene is drawing much interest because of its exceptional geometries and electronic topologies, i.e., excellent conductivity, fast ion diffusion, and hydrophilic nature, which make it a competent material for storage systems. [3]. MXene is a graphene-like layered 2D early transition metal carbide, nitride, or carbonitride that has been prepared by selective etching the A layers from 3D MAX phases ($M_{n+1}AX_n$, where n ranges from 1 to 3). For example, M_2AX , M_3AX_2 , M_4AX_3 ; M denotes a transition metal (e.g., Ti, Nb, Mo, Ta, Sc, V, Zr etc); A is an element from group III-A or IV-A (Al, Si, Ga); and X corresponds to carbides, nitrides, or carbonitride [4]. Because the M–X bond is stronger than the M–A bond, the A atom can be selectively etched to yield 2D MXene [5].

A number of studies have been carried out on Nb_2C , Nb_4C_3 MXenes for their potential use in energy storage devices, catalysis, and biomedical application. Ghidiu *et al.* reported the synthesis and characterization of Nb_4C_3 MXene obtained by selectively etching Nb_4AlC_3 [6]. Shen *et al.* demonstrated the synthesis of Nb_2C MXene and explored its electrochemical performance for supercapacitors [7]. Nishat *et al.* described the electrochemical performance of Nb_2C and Nb_2CO_2 for Na- and Li-ion batteries using an ab initio approach [8]. Although several studies have been conducted on Nb-based MXenes, such as Nb_2C and Nb_4C_3 , studies on Nb_3C_2 remain limited. Furthermore, Cr doping in Nb_2C and Nb_4C_3 MXenes has not yet been explored [6, 7]. In particular, a systematic investigation of its structural stability, electronic, magnetic, and electrochemical properties under transition metal doping, especially with Cr, has not been explored. Hence, a detailed first-principles study is required to evaluate the potential of Cr-doped Nb_3C_2 MXene for high-performance Li-ion battery applications.



Furthermore, niobium-based MXenes show superior performance as an anode material in Li-ion batteries compared to Ti-based MXenes, as reported in the literature [9]. Nb₃C₂ holds a different M/X ratio compared to other members of the MXene family, making it unique and influencing its layer thickness, electron density, surface chemistry, and mechanical strength, thereby positioning it as a promising and versatile candidate for future energy devices [10]. Due to its layered configuration, Nb₃C₂ MXene possesses relatively small interlayer spacing, which hinders the intercalation and deintercalation of Li⁺ ions during battery operation [11]. To overcome this limitation, various dopant atoms have been introduced to expand the interlayer distance and investigate their influence on the electrocatalytic behavior of MXenes [12]. Doping not only increases the lattice parameters but also tunes the band gap and enhances the electrical conductivity, thereby improving the overall electrochemical performance of the material [13]. In recent years, several studies have demonstrated that doping can effectively modify the interlayer spacing and surface chemistry of MXenes, thereby improving their electrochemical performance [14]. Among potential dopants, Cr is notable for its good electrical conductivity and an ionic radius (0.62 Å) closely matching that of niobium (0.64 Å), making it a promising candidate for Nb₃C₂ MXene doping [15].

Herein, a systematic first-principles investigation of pristine Nb₃C₂ and Cr-doped Nb₃C₂ MXene is performed to explore their structural stability, electronic structure, magnetic behavior, transport properties, and electrochemical performance as potential anode materials for Li-ion batteries. Furthermore, the effect of Cr doping on the structural, electronic, and electrochemical properties of Nb₃C₂ is comprehensively examined.

The findings of this work provide valuable theoretical insights into the properties of Nb₃C₂ MXene and highlight the potential of Cr doping to improve its electrochemical performance, thereby supporting future experimental investigations and the development of advanced MXene-based energy storage devices.

2. Computational method

All computational calculations were executed within the density functional theory (DFT) framework, employing the full-potential augmented plane waves plus local orbital (FP-LAPW+lo) method, as implemented through the WIEN2k code [16]. The exchange–correlation potential energies of the electrons were calculated in the generalized gradient approximation (GGA) via Perdew–Burke–Ernzerhof (PBE) functional [17].



The two-dimensional Nb₃C₂ MXene structure was constructed by selectively etching the A-group element from its corresponding MAX phase precursor to obtain a Nb₃C₂ monolayer. A vacuum layer of 15-20 Å was introduced along the c-direction to avoid the interactions between periodic layers. To evaluate the effect of substitutional Cr doping, one Nb atom in the supercell was substituted with a Cr atom. All structures were fully optimized prior to the electronic, magnetic and transport property calculations [2, 6].

Firstly, the unit cell and supercell structure of Nb₃C₂ and Cr-doped Nb₃C₂ were generated and optimized at 1000 (19 × 19 × 2) and 200 k-points within a 2 × 12 × 7 k-mesh in the irreducible Brillouin zone (IBZ), respectively, using GGA-PBE. The expansion of valence wave functions within the Nb spheres was conducted up to $l_{\max} = 10$. Additionally, the Fourier expansion of the charge density was pursued up to $G_{\max} = 14$. For structural and electronic calculations, the potential was expanded within the Nb spheres, employing a combination of spherical harmonic functions and the Brillouin zone. The cut-off energy for the separation of valence and core electrons was chosen as -6 Ry, which corresponds to $RMT K_{\max} = 7$, where RMT is the smallest of all atomic sphere radii and K_{\max} determines the truncation of the reciprocal lattice expansion of the wave functions in the interstitial region [18, 19]. Convergence of the total energy was set to 10⁻⁵ eV between successive iterations, with a Gaussian smearing factor of 0.05 eV. Atomic positions were fully relaxed until the maximum force on each atom was below 10⁻³ eV/Å. The plane-wave basis set was taken with an energy cut-off of 600 eV. For the electronic structure analysis, the Fermi level (EF), defined as the highest occupied electronic state at 0 K, was set to 0 eV as the reference energy [20, 21].

Phonon dispersion calculations were performed using the PHONOPY package interfaced with WIEN2k to evaluate the dynamical stability of pristine and Cr-doped Nb₃C₂ structures. In addition, ab initio molecular dynamics (AIMD) simulations were carried out to examine thermal stability. The AIMD simulations were conducted in the canonical ensemble (NVT) using a Nosé–Hoover thermostat at 500 K. A time step of 1 fs was employed, and the total simulation time was 100 ps, corresponding to 10,000 MD steps [22].

Spin-polarization calculations were carried out to determine the magnetic ordering of the 2D MXenes. Pristine Nb₃C₂ exhibited negligible magnetism (very small magnetic moments within numerical error), while Cr-doping stabilized a ferromagnetic state. The magnetic behavior was further evaluated using both GGA-PBE and GGA-PBE+U, where U represents the Hubbard potential. The U values of Nb (0.22 Ry = 3 eV) [20] and Cr (U = 0.15 Ry = 2 eV) were adopted



from the literature, where similar parameters successfully captured the localized d-electron correlations [23].

Although applying the U slightly increased the bandgap, the valence and conduction band levels near the Fermi level remained consistent, ensuring reliable results for electronic and optical properties [24]. The simplicity of this approach, along with the availability of all required inputs from first principles, makes it highly suitable for high-throughput computations, where it has gained wide acceptance [25]. The electronic transport properties were calculated using the BoltzTraP2 code interfaced with WIEN2k under the constant relaxation time approximation (RTA), yielding the thermal and electrical conductivity [26]. To evaluate the Li storage capability of pristine and Cr-doped Nb_3C_2 for Li-ion batteries, we computed the adsorption energy [27], the open circuit voltage (OCV) [28], and the theoretical capacity (Q) [29].

The adsorption energy (E_{ads}) was determined as:

$$E_{\text{ads}} = \frac{[E_{\text{complex}} - (E_{\text{bare}} + x\mu_{\text{M}})]}{x} \quad (1)$$

The Open-circuit voltage (OCV) was calculated using:

$$V = [E_{\text{total}}(\text{Nb}_3\text{C}_2) + xE_{\text{total}}(\text{Li}) - E_{\text{total}}(\text{Li}_x\text{Nb}_3\text{C}_2)] / x \quad (2)$$

The theoretical capacity (Q) was determined from:

$$Q = nF / M_f \quad (3)$$

Here, $E_{\text{total}}(\text{Nb}_3\text{C}_2)$ and $E_{\text{total}}(\text{Li}_x\text{Nb}_3\text{C}_2)$ denotes the total energies per formula unit before and after Li intercalation, while $E_{\text{total}}(\text{Li})$ is the energy per Li atom in bulk lithium; multiplying by x accounts for the total energy of x intercalated Li atoms during the process. In theoretical capacity formula, 'n' is the number of electrons transferred per formula unit, F is the Faraday constant, and M_f is the mass of the formula unit.

3. Results and discussion

3.1. Structure Predication of Novel MXene

According to results obtained via first-principles DFT calculations, the newly designed Nb_3C_2 MXene structure was found to belong to the hexagonal geometry with space group number 194 (P63/mmc) and lattice parameters $a = b = 3.131 \text{ \AA}$, $c = 19.24 \text{ \AA}$ with $\alpha = \beta = 90^\circ$ and $\gamma = 120^\circ$. Two inequivalent niobium atoms were identified as Nb (1), Nb (2), along with one carbon atom, having fractional coordinates Nb (1) (2/3, 1/3, 0.875), Nb (2) (0, 0, 0.5) and C: (1/3, 2/3, 0.924). The obtained lattice constant values are very close to the reported literature value of 3.3008 \AA [30].



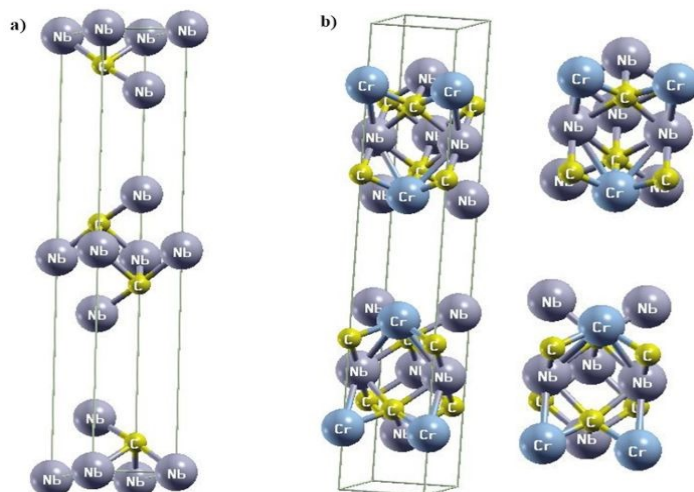


Figure 1. (a) Crystal structure of Pristine Nb_3C_2 . (b) Schematic view of the $2 \times 1 \times 1$ supercell of Cr-doped Nb_3C_2

To elucidate the effect of Cr doping in the Nb_3C_2 structure, a $2 \times 1 \times 1$ supercell was generated. This supercell contains six Nb atoms and two C atoms. A 25% Cr-doped Nb_3C_2 structure was then optimized using 1000 k-points within a $2 \times 12 \times 7$ k-mesh in the irreducible Brillouin zone (IBZ). The schematic views of pristine and Cr-doped Nb_3C_2 are shown in Figure 1.

3.2. Structural and Thermal Stability

The phonon dispersion curves for both pristine and Cr-doped Nb_3C_2 are represented in the Figure 2. It is evident that no imaginary (negative) frequencies are present throughout the Brillouin zone, confirming the dynamical stability of both structures. A slight shift in phonon band separation is observed in the frequency range of approximately 10–15 THz between pristine and doped Nb_3C_2 (Figure 2a and 2b), indicating modifications in interatomic interactions and bonding strength due to doping. Both systems exhibit three acoustic and several optical branches, as typically observed in two-dimensional materials.

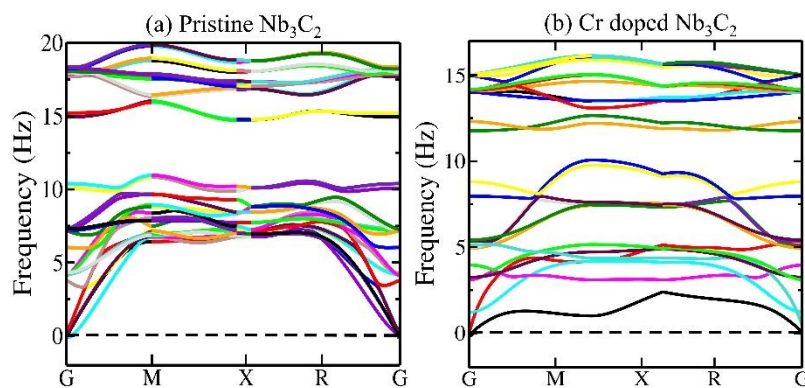


Figure 2. Phonon dispersion curves of (a) pristine Nb_3C_2 and (b) Cr-doped Nb_3C_2 MXenes



The slope of the acoustic branches is slightly higher in pristine Nb_3C_2 as shown in Figure 2a, compared to the doped structure in Figure 2(b), suggesting a relatively higher phonon group velocity. Furthermore, the absence of a distinct gap between acoustic and optical modes may enhance acoustic–optical phonon scattering, which can influence the thermal conductivity of both pristine and doped Nb_3C_2 MXene layers [31].

The energy evolution of pristine and Cr-doped Nb_3C_2 MXene systems during the AIMD simulations is presented in Figure 3, with pristine Nb_3C_2 shown in Figure 3a and Cr-doped Nb_3C_2 in Figure 3b. The total energy of both structures remains nearly constant throughout the simulation, indicating good numerical stability. The potential, kinetic, and non-bonding energies exhibited moderate fluctuations around their average values, which are expected due to the thermal motion of atoms. For pristine Nb_3C_2 (Figure 3a), energy variations remain confined within a narrow range over the 10 ps simulation, suggesting that the structural framework remains intact without significant distortion. A similar trend is observed for the Cr-doped Nb_3C_2 system (Figure 3b), where the energy components fluctuate around equilibrium values without any noticeable drift in total energy. These stable energy oscillations confirm that Cr incorporation does not compromise the structural integrity of the MXene lattice, demonstrating that both systems maintain thermal stability under the simulated conditions [22].

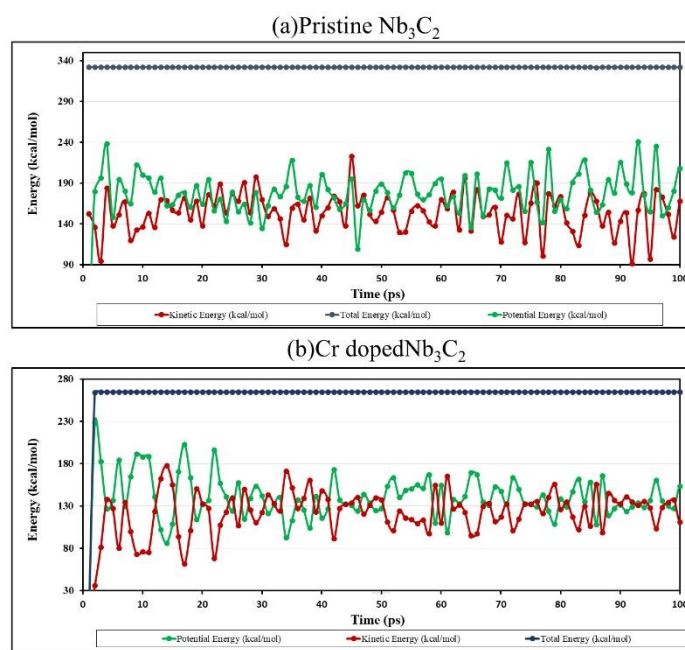


Figure 3. AIMD simulation of (a) Pristine Nb_3C_2 and (b) Cr-doped Nb_3C_2 at 500 K, showing energy evolution with atoms in their most stable position



3.3. Electronic Properties of Pristine and Cr-doped Nb₃C₂

Exploring the electronic properties of a potential electrode requires determining whether the material exhibits metallic, semiconducting, or insulating behavior [32]. In this study, Cr atoms were employed as dopants to investigate the electronic characteristics, including charge density distribution, band structure, and density of states (DOS). The energy gaps between valence and conduction bands were identified from the calculated density of states (DOS) and band structure [33].

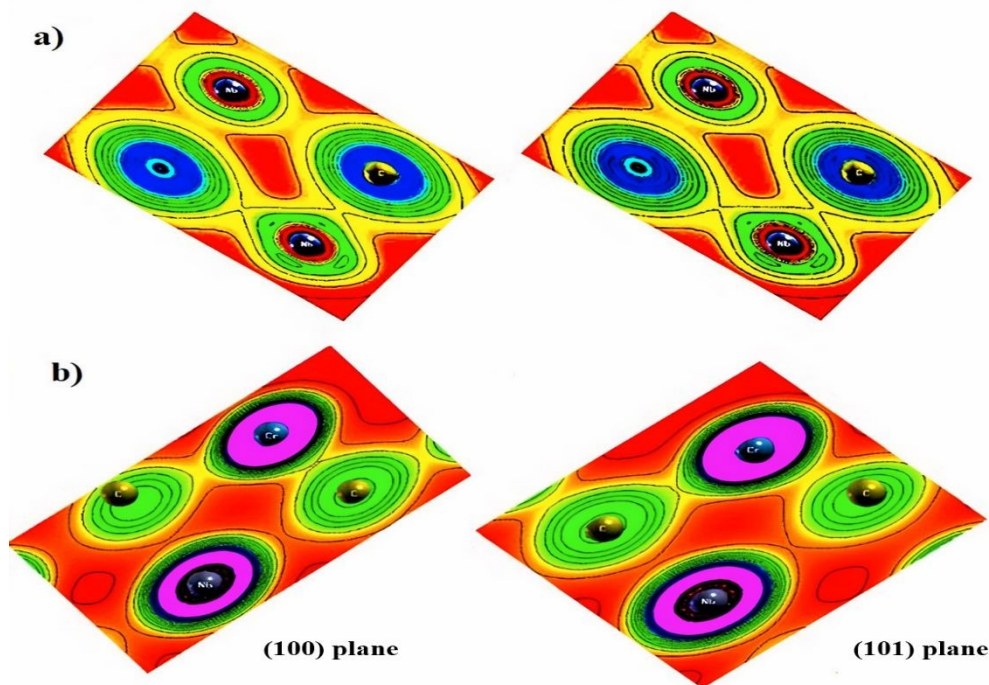
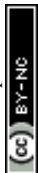


Figure 4. Charge density distribution of (a) Pristine Nb₃C₂ and (b) Cr doped Nb₃C₂ along the (100) plane and (110) crystallographic planes. The plots illustrate charge localization and bonding characteristics between Nb-C and Nb-Cr atoms, highlighting the electronic modification of electronic interactions upon Cr doping.

Charge density plots provide direct insight into the bonding characteristics of the system [34]. Figure 4(a, b) shows the electron density of pristine and Cr-doped Nb₃C₂ along the (100) and (110) planes. It is revealed that Cr-doping modifies the bonding nature between Nb and C atoms. As shown in Figure 4(a), the charge density contour of pristine Nb₃C₂ indicates a covalent bond between C and Nb atoms, while in Figure 4(b), the Cr-doped Nb₃C₂ exhibits a covalent bond between Cr and C atoms due to the overlap of their valence electrons. In addition, the spherical charge distribution around Nb atoms in Nb₃C₂ indicates ionic bonding between the electronegative C atoms and electropositive Nb atoms. In the Cr-doped Nb₃C₂, the weak covalent interaction between Nb and C atoms suggests a weaker hybridization tendency of Nb towards C,



as compared with pristine Nb_3C_2 [35]. These features confirm that Cr doping significantly alters the bonding environment and electronic interactions in Nb_3C_2 .

The interpretation of the band structure provides detailed insights into the electronic behaviour of materials, serving as a fundamental indicator of their conductivity and their responsiveness to doping-induced modifications. The band structure of pristine Nb_3C_2 (Figure 5a) indicated metallic behavior, as the band gap was found to be zero [36].

In contrast, Cr-doping (Figure. 3b) increased the density of electronic states around the Fermi level; however, the band gap for Cr doped Nb_3C_2 structure also remained zero. This confirms that Nb_3C_2 retains its metallic character even after Cr doping. Moreover, Cr doping increases the electronic states above the Fermi level due to the additional energy levels introduced by Cr atoms within the crystal lattice, as evident from Figure 5b [37].

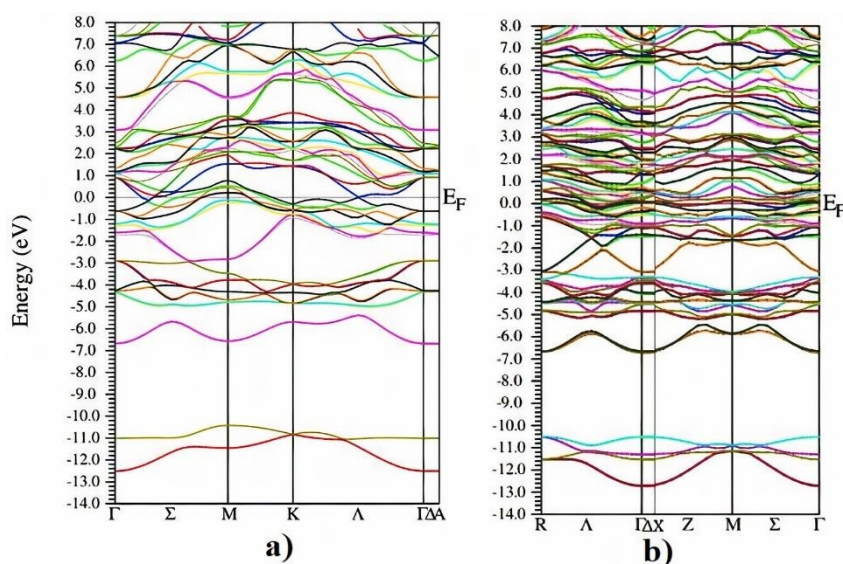


Figure 5. Band Structure of (a) pristine Nb_3C_2 calculated using sp-GGA, and (b) Cr-doped Nb_3C_2

This expansion is shown n-type doping effect of Cr atoms, bringing about distinct modifications in the pristine Nb_3C_2 band structure, which in turn influences the electrical conductivity of the material [38]. Band gap analysis therefore suggests that both pristine and doped Nb_3C_2 exhibit effective electrical conductivity, as this enables efficient electron transport during electrochemical processes [39].

To estimate the number of states at different energy levels occupied by electrons, the partial and total density of states (PDOS & TDOS) for pristine and Cr-doped Nb_3C_2 were calculated, as shown in Figures 6 and 7, respectively. For the TDOS, Figure 6(a) shows a maximum peak in the



density of states around -6.5 eV, indicating a high concentration of electrons at this energy level [40].

For the PDOS of pristine Nb_3C_2 (Figures 6a–d), the maximum electronic states at the Fermi level (E_F) mainly originate from the Nb_1 -4d orbital states [41]. The valence band is dominated by C-2p states, with an admixture of Nb d-orbital contributions, confirming covalent Nb-C bonding [42]. Above the Fermi level, the conduction band is primarily composed of Nb1-4d orbitals, with additional contributions from Nb2-4d states, suggesting anisotropic electronic transport [43]. The dominance of Nb-4d orbitals near the Fermi level confirms its metallic conductivity, which is beneficial for electrochemical performance when used as an electrode material [42].

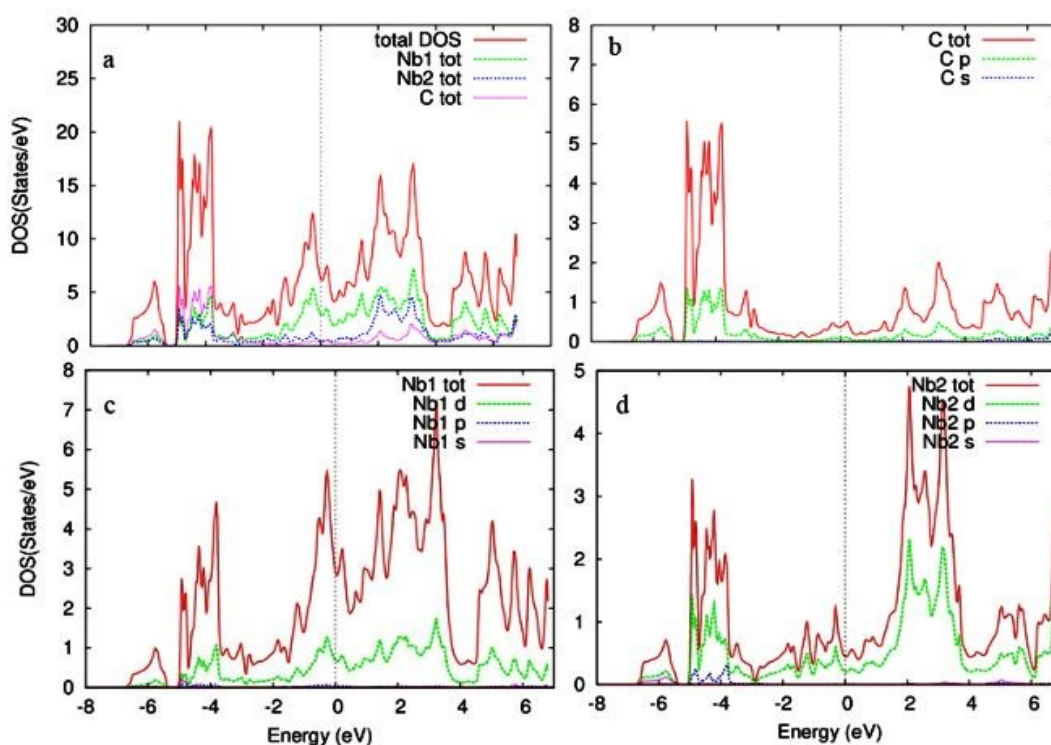


Figure 6. (a) Total density of states (TDOS) of pristine Nb_3C_2 , and (b–d) partial density of states (PDOS) of C, Nb_1 , Nb_2 atoms, respectively.

Cr doping significantly increases the density of states per electron volt. At the Fermi level, the dominant contributions arise from Cr_1 -3d and Cr_2 -3d orbitals, with smaller contributions from Nb_1 -4d and Nb_2 -4d states. The upper part of the conduction band consists of states from Cr_1 , Cr_2 , Nb_1 , Nb_2 , Nb_3 , and Nb_4 d orbitals. In the energy range of 2–4 eV above E_F , the conduction band is mainly dominated by Nb_3 -4d and Nb_4 -4d orbitals, with minor contributions from Cr_1 -3d, Cr_2 -3d, and Nb_1 -4d and Nb_2 -4d states. Meanwhile, C-2p orbitals contribute negligibly to the



conduction band but play a major role in the valence band through hybridization with Nb₃-4d and Nb₄-4d orbitals.

As evident from Figure 7, the density of states in both the valence and conduction bands cross the

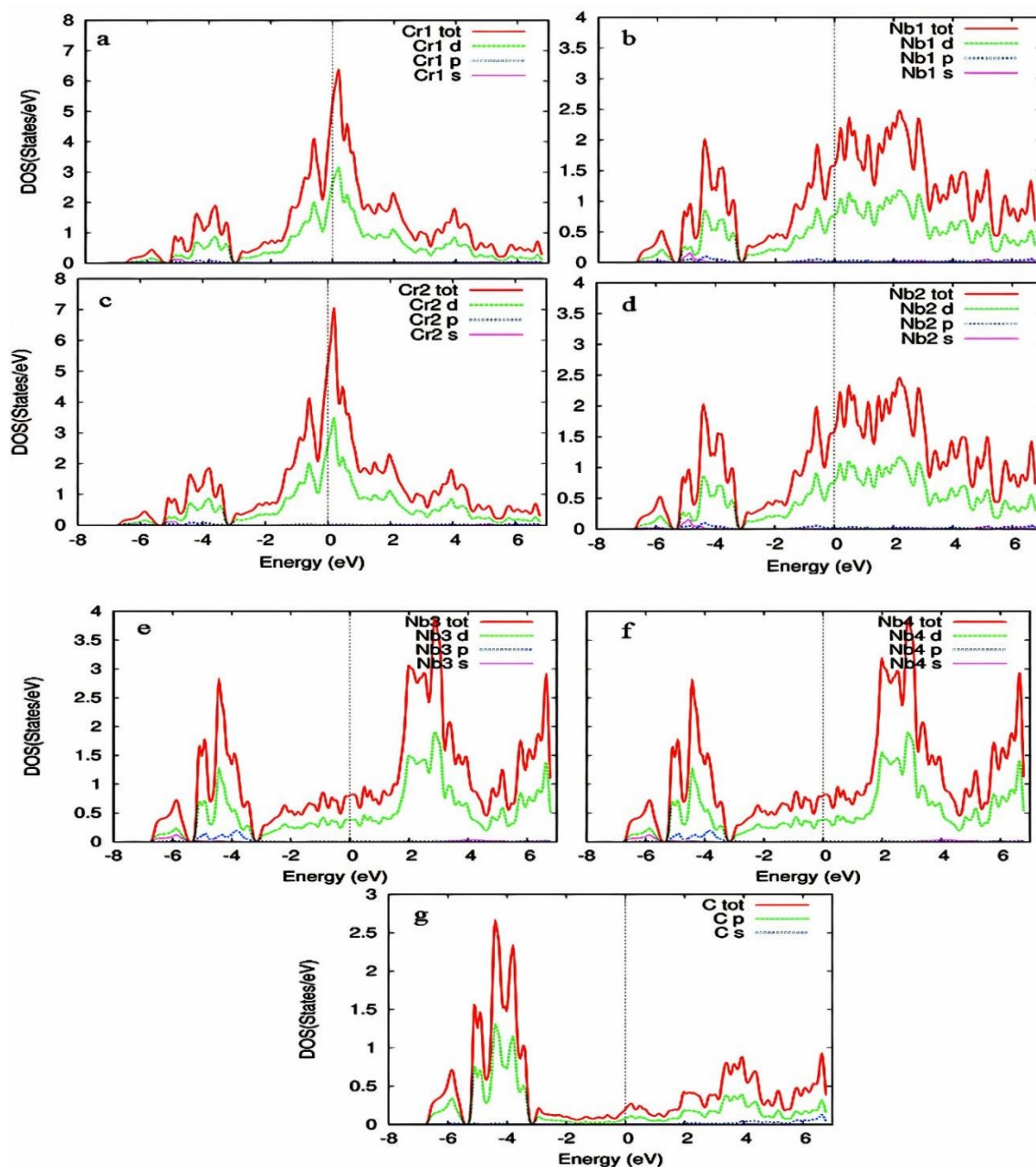


Figure 7. Partial Density of States (PDOS) of Cr-doped Nb₃C₂ in a 2x1x1 Supercell:(a) Cr₁, (b) Nb₁,(c) Cr₂,(d) Nb₂, (e) Nb₃, (f) Nb₄, (g) C atoms.

Fermi level without opening a gap, thereby confirming the metallic character of Cr-doped Nb₃C₂ [45]. The PDOS plots show the orbital contributions of Cr, Nb, and C atoms in Cr-doped Nb₃C₂. Cr atoms (a, c) mainly contribute through d-states near the Fermi level, indicating strong hybridization. Nb atoms (b–f) also show dominant d-orbital contributions, crucial for electronic



conductivity. C atoms (g) contribute primarily through p-states, supporting the overall electronic interaction in the heterostructure.

3.4. Magnetic Properties

Magnetism in MXene has not been extensively explored for the M_3C_2 phase, either theoretically or experimentally. For comparison, Ti_3C_2 magnetism has been briefly studied by Shien et al., who reported ferromagnetic behavior [46, 47].

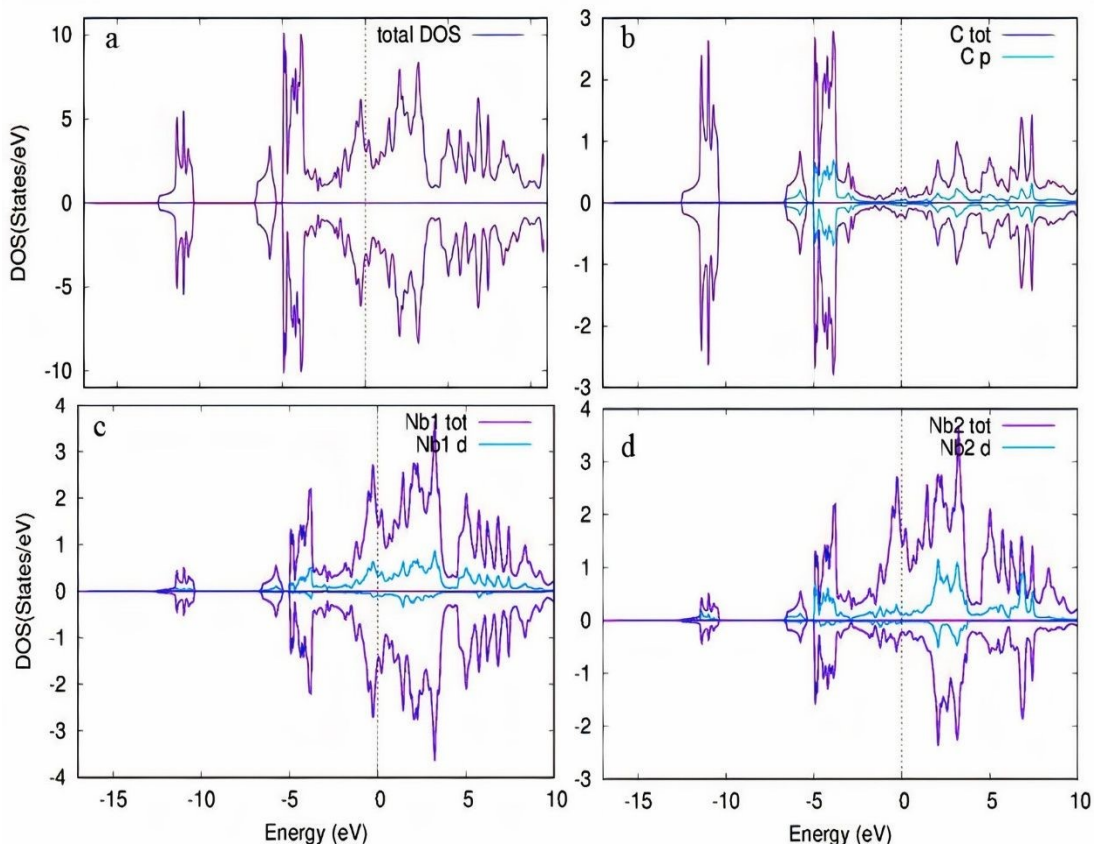


Figure 8. Density of states (DOS) of pristine Nb_3C_2 calculated using spin-polarized GGA (sp-GGA): (a) total DOS (TDOS), (b) DOS and PDOS of C-2p states, (c) TDOS and PDOS of Nb1-4d states, (d) TDOS and PDOS of Nb2-4d states

Herein, pristine Nb_3C_2 exhibited an essentially non-magnetic ground state, as the calculated magnetic moments for Nb_2 were $-0.00002 \mu_B$ (GGA) and $-0.00007 \mu_B$ (GGA+U), which are negligibly small and within the margin of computational error [48]. Although the PDOS of Nb_2 shows a slight asymmetry between spin-up and spin-down states (Figure 8a), the imbalance is too weak to generate a measurable magnetic response in the whole compound. Consequently, the net magnetic moment is effectively zero, confirming the non-magnetic nature of pristine Nb_3C_2 .

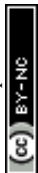


Figure 8(b-d) further illustrates the DOS and PDOS of C-2p, Nb1-4d, and Nb2-4d states. By applying the Hubbard potential (GGA+U), the magnetic moment of the carbon atom became aligned with that of Nb2 and anti-parallel to Nb1, which enhanced the overall magnetic moment. This increase arises because the GGA+U correction shifts the partial density of states of Nb1 and Nb2, accounting for stronger electron-electron correlation effects [49] as shown in Figure 9. Cr doping in Nb₃C₂ enhanced the magnetism and stabilized a ferromagnetic ground state.

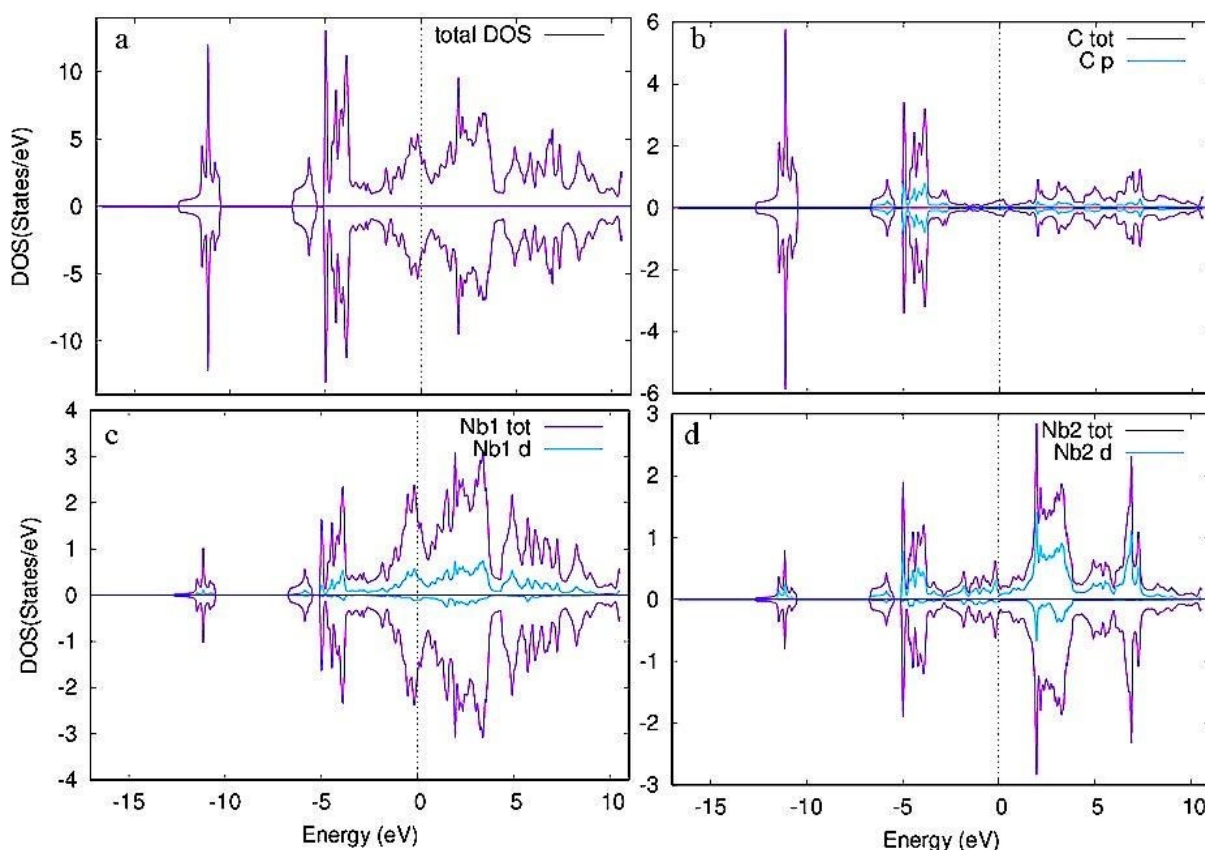


Figure 9. Density of states (DOS) of pristine Nb₃C₂ calculated using spin-polarized GGA with Hubbard U correction (sp-GGA+U): (a) total DOS (TDOS), (b) TDOS and PDOS of C-2p states, (c) TDOS and PDOS of Nb₁-4d states, and (d) TDOS and PDOS of Nb₂-4d states.

Table 1 shows that pristine Nb₃C₂ is nearly non-magnetic, with negligible total magnetic moment under both PBE-GGA and PBE-GGA+U calculations. Upon Cr doping, the system exhibits a substantial increase in magnetism (total moment rising from ~7.5 to ~12.0 μ B), primarily originating from the strong spin polarization of Cr-3d states and significant interstitial contributions, while Nb and C atoms provide smaller site-dependent moments. Figure 8 further supports this, as the spin-polarized PDOS confirms the ferromagnetic nature through asymmetry of electronic states below and above the Fermi level for majority and minority spin channels [50]. The Cr-d orbitals (Fig. 10c, d) dominate the magnetism with strong spin polarization,



whereas C-p orbitals (Fig. 10b) remain nearly symmetric. Nb-d states (Fig. 10e–h) display moderate asymmetry, indicating induced contributions through hybridization with Cr-d states. Overall, the net magnetic moment mainly arises from unpaired Cr-d electrons, with Nb atoms providing secondary polarization, thereby stabilizing robust ferromagnetism in Cr-doped Nb_3C_2 , which is beneficial for charge storage and transport in lithium-ion batteries.

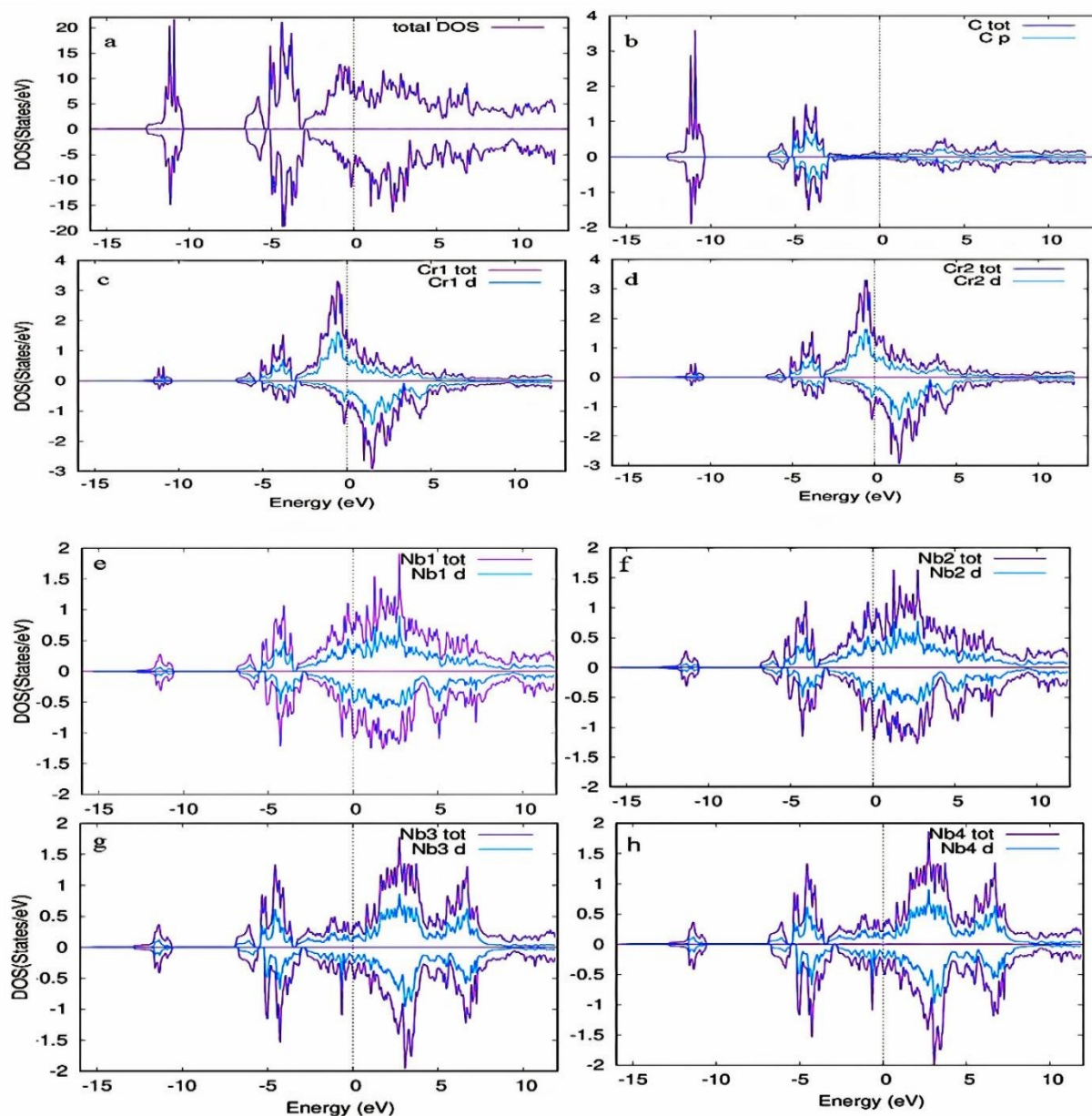
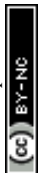


Figure 10. Density of states (DOS) for Cr-doped Nb_3C_2 calculated using sp-GGA: (a) total DOS, (b) TDOS and PDOS of C-2p states, (c-d) TDOS and PDOS for Cr1, Cr2 (total and 3d states, respectively), and (e-h) TDOS and PDOS for Nb1, Nb2, Nb3 and Nb4 (total and 3d states, respectively).



The calculated magnetic moment values for pristine Nb₃C₂ and Cr-doped Nb₃C₂ are summarized in Table 1.

Table 1. Magnetic moments of pristine Nb₃C₂ and Cr-doped Nb₃C₂

Compound	Atoms	Magnetic Moment	Magnetic Moment
		(PBE-GGA)	(PBE-GGA+U)
Pristine Nb ₃ C ₂	Nb1 (μ _B)	0.00003	0.00026
	Nb2 (μ _B)	-0.00002	-0.00007
	C (μ _B)	0.00001	-0.000001
	Interstitial (μ _B)	0.00013	0.00059
	Total (μ _B)	0.00024	0.00146
Cr-doped Nb ₃ C ₂	Cr1(μ _B)	1.76157	2.51618
	Cr2(μ _B)	1.76010	2.55740
	Nb1-Nb4(μ _B)	-0.03548	0.11141
		-0.03698	0.16468
		-0.02989	-0.07683
		-0.02989	-0.07441
	C(μ _B)	-0.04485	-0.07782
		-0.04473	-0.08433
		-0.01336	-0.02645
		-0.01323	-0.03146
Interstitial (μ _B)	0.94320	2.08746	
Total (μ _B)	7.48972	12.04418	

3.5. Transport Properties

The transport properties, including electrical conductivity, Seebeck coefficient, and thermal conductivity, were evaluated as functions of chemical potential at temperatures of 300 K, 500 K, and 700 K. These parameters provide insight into the charge-carrier behavior and electron



transport efficiency in Nb_3C_2 , which is essential for assessing its potential as an electrode material for energy storage applications [51]. Transport properties were also estimated for the lithiated systems of both pristine and Cr-doped Nb_3C_2 , since lithiation and delithiation during Li-ion battery charge/discharge significantly influence charge-carrier mobility and the density of states near the Fermi level [52].

The Seebeck coefficient is a key parameter for understanding charge-carrier behavior and transport efficiency [53]. Figure 11 depicts the Seebeck coefficient as a function of chemical potential for various Nb_3C_2 -based compounds. For pristine Nb_3C_2 , Figure 11(a) shows four distinct peaks at chemical potentials of -5.9 eV, -5.2 eV, -3.2 eV,

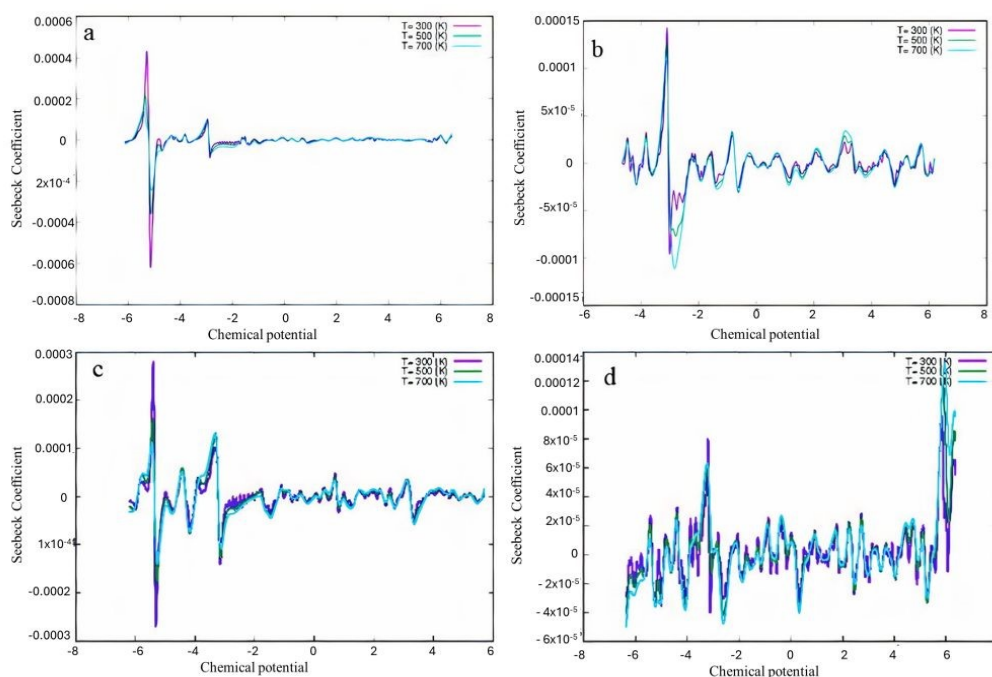


Figure 11. Seebeck coefficient as a function of chemical potential at three different temperatures for the compounds: (a) pristine Nb_3C_2 , (b) $\text{Li}_2\text{Nb}_3\text{C}_2$, (c) Cr-doped Nb_3C_2 , and (d) Li_4 -Cr-doped Nb_3C_2 .

and -3.0 eV. Outside this range, the Seebeck coefficient rapidly approaches zero, which indicates good transport performance. In contrast, lithiated Nb_3C_2 , Cr-doped Nb_3C_2 , and lithiated Cr-doped Nb_3C_2 Figure 11 (b-d) show smaller Seebeck values over the entire chemical potential range, consistent with strong metallic behavior. In Li-ion battery electrodes, metallic conductivity is essential for efficient charge transport [54]. These results suggest that the lithiated phases, particularly $\text{Li}_2\text{Nb}_3\text{C}_2$, and Li_4 Cr-doped Nb_3C_2 , exhibit high metallic conductivity and may provide more efficient electronic transport during Li-ion battery operation compared to pristine Nb_3C_2 .



The maximum values of the Seebeck coefficient for the different compounds at various temperatures are summarized in Table 2. The results show that, with increasing temperature, the carrier concentration increases, leading to a reduction in the Seebeck coefficient, as expected for metallic systems. This behavior is consistent with the metallic nature of all compounds.

Table 2. Seebeck Coefficient at different temperatures for lithiated and de-lithiated phases of pristine and Cr-doped Nb₃C₂.

Temperature (K)	Nb ₃ C ₂	Li ₂ Nb ₃ C ₂	Cr-doped Nb ₃ C ₂	Li ₄ CrNb ₃ C ₂
300	4.2×10^{-4}	1.5×10^{-4}	2.9×10^{-4}	8.0×10^{-5}
500	2.0×10^{-4}	1.3×10^{-4}	1.8×10^{-4}	6.5×10^{-5}
700	1.0×10^{-4}	1.2×10^{-4}	1.2×10^{-4}	6.0×10^{-5}

Electrical conductivity reflects the ease of electron flow in a material, and materials with efficient transport typically exhibit high conductivity. In metallic systems, conductivity generally decreases with increasing temperature but increases with chemical potential, due to higher carrier concentration and improved mobility [53]. As shown in Figures 12a and 12c, the electrical conductivity approaches zero near -5.5 eV at 300 K for both delithiated Nb₃C₂ and delithiated Cr-doped Nb₃C₂. In contrast, the lithiated phases Figure. 12(b) & 12(d) exhibited significantly higher conductivity than their delithiated counterparts, indicating enhanced electron conduction during Li-ion battery operation. The maximum values of electrical conductivity are summarized in Table. 3.

Table 3. Electronic conductivity of lithiated and delithiated phases of pristine and Cr-doped Nb₃C₂ at room temperature.

Compound	Electrical Conductivity (S/m)
Li ₂ Nb ₃ C ₂	4.7×10^{20}
Nb ₃ C ₂	4.4×10^{20}
LiCr-Nb ₃ C ₂	1.9×10^{20}
Cr-Nb ₃ C ₂	1.7×10^{20}

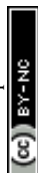
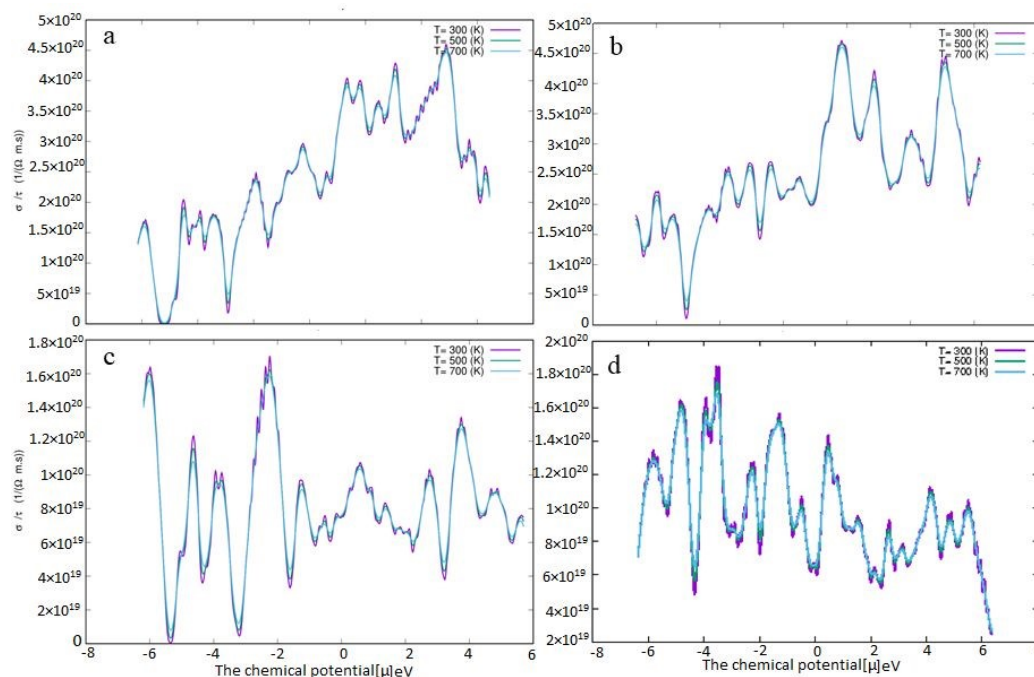


Figure 11. Electronic conductivity as a function of chemical potential at three different

temperatures for : (a) pristine Nb₃C₂, (b) Li₂Nb₃C₂, (c) Cr-doped Nb₃C₂, and (d) Li₄-Cr-doped Nb₃C₂.

Figure 13 depicts the thermal conductivity of Nb₃C₂-based systems as a function of chemical potential at three different temperatures. For all compounds, κ increases with temperature, consistent with their metallic nature [56]. Pristine Nb₃C₂ shows a smoother variation in thermal conductivity with chemical potential, whereas the other systems exhibit stronger variations, maintaining higher conductivity over a broader chemical potential (μ) range. Combined with the Seebeck coefficient and electrical conductivity results, these trends indicate that lithiation significantly enhances both charge and heat transport [57]. In particular, Li₂Nb₃C₂ and Li₄-Cr-doped Nb₃C₂ demonstrate excellent transport properties, making them promising candidates for efficient Li-ion battery electrodes.



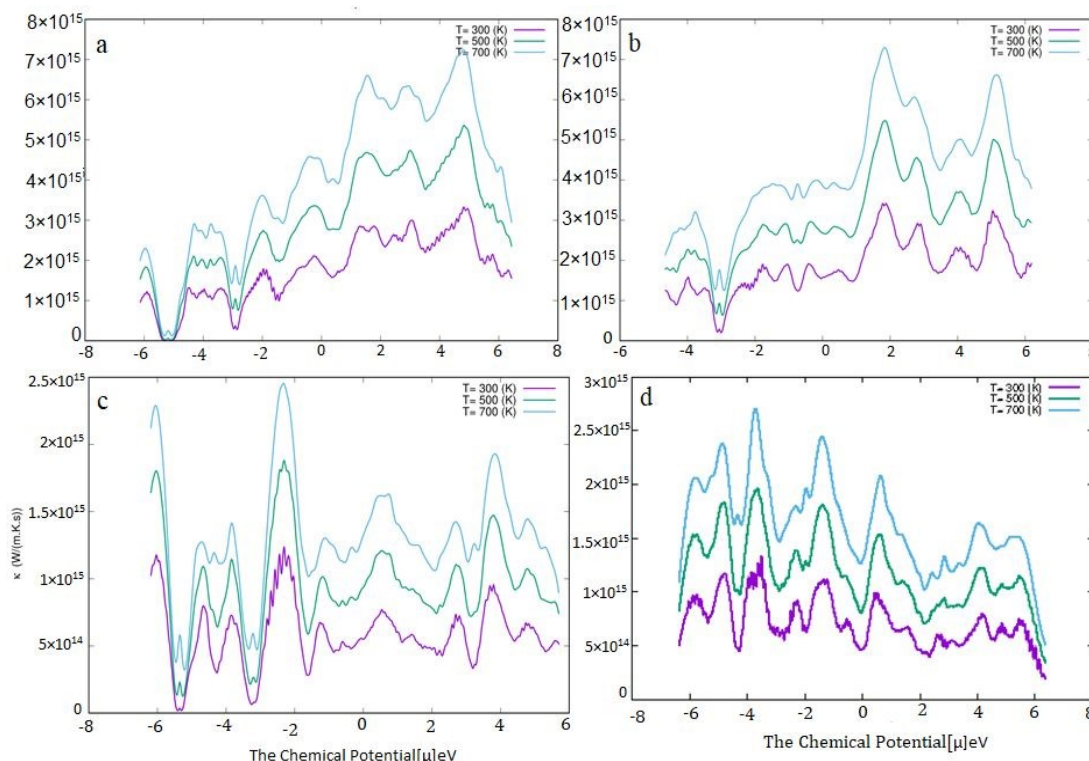


Figure 13. Thermal Conductivity as a function of chemical potential at three different temperatures for the compounds: (a) pristine Nb_3C_2 , (b) $\text{Li}_2\text{Nb}_3\text{C}_2$, (c) Cr-doped Nb_3C_2 , and (d) Li_4 -Cr-doped Nb_3C_2 .

3.6. Electrochemical Performance of MXene as an Electrode Material

Metallic behavior is a desirable characteristic for electrode materials [58]. The electronic properties confirm that both pristine Nb_3C_2 and Cr-doped Nb_3C_2 are metallic, thereby fulfilling this requirement. In electrochemical applications, intercalating species play a crucial role, with Li^+ ions being the most widely used in Li-ion batteries [59]. In this study, Li^+ intercalation into pristine Nb_3C_2 and Cr-doped Nb_3C_2 MXene was investigated to evaluate their storage capability as electrode materials. The electrochemical suitability of these MXenes was examined through adsorption energy analysis.

3.6.1. Adsorption Energy

Equation (1) was employed to calculate the adsorption energies of lithium ions adsorbed on pristine and Cr-doped Nb_3C_2 . The adsorption energy was further used to estimate the average intercalation potential of the materials [60]. In this study, the calculated adsorption energies of a Li atom on pristine Nb_3C_2 and Cr-doped Nb_3C_2 were -1.20 eV and -1.48 eV, respectively. A



negative value of E_{ad} indicates that the corresponding atom favors adsorption on the surface rather than forming clusters [61, 62]. Cr-doped Nb_3C_2 exhibits a more negative adsorption energy, indicating that Li adsorption is energetically more favorable compared to pristine Nb_3C_2 . Similar trends have been reported in other doped MXenes; for instance, V-doped Ti_2Co_2 shows more negative energies in the range of -1.9 eV to -2.8 eV compared to its undoped system [63]. This behavior is attributed to the additional electronic states introduced by the dopant atoms, which enhance charge transfer and orbital hybridization with Li, thereby strengthening the binding interaction [64]. In the present case, the introduction of Cr atoms modifies the electronic density of states near the adsorption site, increasing the interaction with Li atoms and thereby improving adsorption favorability. According to our calculations, a unit cell and a $2 \times 1 \times 1$ supercell can accommodate only 2 and 4 Li atoms per formula unit, respectively. Beyond the adsorption of two Li ions per formula unit, the system reaches a saturation point. The saturation point in a structure varies depending on Coulombic repulsion, structural distortion, and the lack of favorable adsorption sites [65].

3.6.2. Open Circuit Voltage (OCV)

The open-circuit voltage (OCV) is an important parameter for evaluating the electrochemical performance of electrode materials in lithium-ion batteries. It provides insights into the average lithiation potential of the material, which directly influences both energy density and cycling stability [66]. In this work, the OCV was determined using Equation (2) for pristine and Cr-doped Nb_3C_2 systems with the adsorption of 2 and 4 Li atoms per formula unit, respectively.

$$V = [E_{total}(Nb_3C_2) + xE_{total}(Li) - E_{total}(Li_2Nb_3C_2)] / x$$

(4)

$$V = [E_{total}(CrNb_3C_2) + xE_{total}(Li) - E_{total}(Li_4CrNb_3C_2)] / x$$

(5)

Here, $E_{total}(Nb_3C_2)$ and $E_{total}(Li_2Nb_3C_2)$ represent the total energies per formula unit of pristine Nb_3C_2 without and with Li intercalation, respectively. Similarly, $E_{total}(Li_4CrNb_3C_2)$ and $E_{total}(CrNb_3C_2)$ correspond to the total energies of the Cr doped system before and after Li intercalation, respectively. $E_{total}(Li)$ denotes the total energy of an isolated Li atom [67].

The corresponding intercalation reactions can be expressed as:



(6)





The calculated OCV for Li⁺ extraction is 1.20 V for Li₂Nb₃C₂ and 1.48 V for Li₄CrNb₃C₂. The positive voltages indicate energetically favorable Li intercalation. Notably, Cr-doped Nb₃C₂ exhibits a higher OCV compared to the pristine system. This enhancement can be attributed to the additional electronic states introduced by Cr atoms, which strengthen the interaction with Li and stabilize the intercalated structure. These values are consistent with previously reported OCV values for other MXene materials; for example, Ti₂C exhibits an OCV of approximately 1.22 V [68].

3.6.3. Theoretical Capacity

The theoretical capacity is a key property of energy storage materials. Here, the theoretical capacity (Q) was estimated using Equation (3) for both pristine and Cr-doped Nb₃C₂ systems.

The theoretical capacity of pristine Nb₃C₂ for Li-ion batteries was found to be 169 mAh g⁻¹, which is comparable to the reported value of Nb₂C (170 mAh g⁻¹) [69]. In contrast, Cr-doped Nb₃C₂ exhibits a significantly higher storage capacity of 280 mAh g⁻¹, indicating that Cr doping substantially enhances the Li-ion storage performance of the MXene.

4. Conclusions

Using first-principles calculations, we systematically investigated the structural, electronic, magnetic, and transport properties of pristine Nb₃C₂ and Cr-doped Nb₃C₂, as well as their potential as electrode materials for Li-ion batteries. Structural analysis confirmed that Nb₃C₂ and Cr-doped Nb₃C₂ adopt hexagonal (P63/mmc) and orthorhombic (Pmm2) crystal structures, respectively. Phonon and AIMD results confirm that both pristine Nb₃C₂ and Cr-doped Nb₃C₂ are dynamically and thermally stable, with no significant structural distortions observed. These findings validate the reliability of the subsequent electronic and magnetic property calculations. Charge density contours revealed that Cr doping substantially modifies the Nb-C bonding nature, while the band structures and density of states (DOS) confirm metallic behavior (indirect zero-band gap) in both systems, primarily originating from Nb 4d states. Moreover, substitutional Cr doping transforms non-magnetic pristine Nb₃C₂ into a ferromagnetic material with a finite magnetic moment, making it a promising candidate for 2D spintronic applications.

Transport property evaluations based on Boltzmann transport theory demonstrate that lithiation significantly enhances charge and heat transport. In particular, Li₂Nb₃C₂ and Li₄Cr-doped Nb₃C₂ exhibit high electrical and thermal conductivities with low Seebeck coefficients, confirming their



metallic character and suitability as Li-ion battery electrodes. Furthermore, Cr-doped Nb₃C₂ outperforms pristine Nb₃C₂, suggesting superior transport performance for high-efficiency energy storage applications.

Electrochemical analysis further supports Cr-doped Nb₃C₂ as a promising electrode material, owing to its higher electronic conductivity, higher open-circuit voltage, and improved theoretical capacity compared to pristine Nb₃C₂. These improved electrochemical and transport properties make Cr-doped Nb₃C₂ a potential candidate for high performance lithium-ion battery electrodes, particularly in applications requiring fast charge transport and high energy density, such as portable electronic devices and electric vehicles. Overall, these findings demonstrate that Cr doping is an effective strategy for tailoring the properties of Nb₃C₂ MXenes, underscoring their strong potential for next-generation spintronic and energy storage applications.

5. Acknowledgments

Authors gratefully acknowledge the School of Interdisciplinary Engineering & Science (SINES) Islamabad, National University of Science and Technology for providing computational resources and facilities to support this work.

6. Conflict of interest

The authors declare that the research was conducted in the absence of any commercial or financial relationships that could be construed as a potential conflict of interest.

7. Data availability

The data that support the findings of this study are available upon request.

8. References

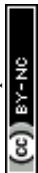
1. Zhang, B.; Huang, Y.; Bao, W.; Wang, B.; Meng, Q.; Fan, L.; Zhang, Q.; Two-Dimensional Stable Transition Metal Carbides MnC and NbC with Prediction and Novel Functionalizations, *RSC Adv.*, **2018**, *8*, 12345–12356, DOI: 10.1039/C8RA12345A.
2. Zhang, X.; Zhang, Z.; Zhou, Z.; MXene-based materials for electrochemical energy storage, *J. Energy Chem.*, **2018**, *27*, 73–85. DOI: 10.1016/j.jechem.2017.08.004.
3. Jhon, Y. I.; Han, I. K.; Lee, J. H.; Jhon, Y. M.; Microscopic understanding of exceptional orientation-dependent tensile and fracture responses of two-dimensional transition-metal carbides, *Appl. Surf. Sci.*, **2022**, *585*, 152557. DOI: 10.1016/j.apsusc.2021.152557.
4. Pang, J.; Mendes, R. G.; Bachmatiuk, A.; Zhao, L.; Ta, H. Q.; Gemming, T.; Liu, H.; Liu, Z.; Rummeli, M. H.; Applications of 2D MXenes in energy conversion and storage systems, *Chem. Soc. Rev.*, **2019**, *48*, 72–133. DOI: 10.1039/C8CS00324F.



5. Zaheer, A.; Zahra, S. A.; Iqbal, M. Z.; Mahmood, A.; Khan, S. A.; Rizwa, S.; Nickel-adsorbed two-dimensional Nb₂C MXene for enhanced energy storage applications, *RSC Adv.*, **2022**, *12*, 4624–4633. DOI: 10.1039/D2RA00014H.
6. Ghidui, M.; Naguib, M.; Shi, C.; Mashtalir, O.; Pan, L. M.; Zhang, B.; Yang, J.; Gogotsi, Y.; Billinge, S. J. L.; Barsoum, M. W.; Synthesis and characterization of two-dimensional Nb₄C₃ (MXene), *Chem. Commun.*, **2014**, *50*, 9517–9520. DOI: 10.1039/C4CC03366C.
7. Shen, B.; Liao, X.; Zhang, X.; Ren, H.-T.; Lin, J.-H.; Lou, C.-W.; Li, T.-T.; Synthesis of Nb₂C MXene-based 2D layered structure electrode material for high-performance battery-type supercapacitors, *Phys. Chem. Chem. Phys.*, **2020**, *22*, 23900–23908. DOI: 10.1039/D0CP03726A.
8. Sultana, N.; Amin, A. A.; Payton, E. J.; Kim, W. K. Insights into Nb₂C and Nb₂CO₂ as high-performance anodes for sodium- and lithium-ion batteries: An *ab initio* investigation, *arXiv*, **2025**, arXiv:2504.08953. DOI: 10.48550/arXiv.2504.08953.
9. Kalsoom, U., Khan, S., Kashif, M., Yaseen, H.S., Hussain, S.A., Azizi, S. and Maaza, M., **2025**. MXene-based hybrid composites for lithium-ion batteries: advances in synthesis strategies and electrochemical performance. *Ionics*, pp.1-21.
10. Akhter, R.; Maktedar, S. S. MXenes: a comprehensive review of synthesis, properties, and progress in supercapacitor applications, *J. Materiomics*, **2023**, *9*(6), 1196–1241. DOI: 10.1016/j.jmat.2023.08.011.
11. Jiang, J.; Zou, Y.; Arramel; Li, F.; Wang, J.; Zou, J.; Li, N.; Intercalation engineering of MXenes towards highly efficient photo(electrocatalytic) hydrogen evolution reactions, *J. Mater. Chem. A*, **2021**, *9*, 24195–24214. DOI: 10.1039/D1TA07332J.
12. Wang, Z.; Dong, Z.; Wu, B.; Wang, Z.; Qiu, Z.; Wang, D.; Zeng, Q.; Liu, X.; Hui, K. N.; Liu, Z.; Zhang, Y. Unlocking the critical roles of N, P co-doping in MXene for lithium–oxygen batteries: elevated d-band center and expanded interlayer spacing, *J. Colloid Interface Sci.*, **2024**, *676*, 368–377. DOI: 10.1016/j.jcis.2024.07.138.
13. Arole, K.; Pas, S. E.; Thakur, R. M.; Amiouny, L. A.; Kabir, M. H.; Dujovic, M.; Radovic, M.; Lutkenhaus, J. L.; Green, M. J.; Liang, H. Effects of intercalation on ML-Ti₃C₂Tz MXene properties and friction performance, *ACS Appl. Mater. Interfaces*, **2024**, *16*(46), 60538–60548. DOI: 10.1021/acsami.4c12157.
14. Qian, H., Ren, H., Zhang, Y., He, X., Li, W., Wang, J., Hu, J., Yang, H., Sari, H.M.K., Chen, Y. and Li, X., **2022**. Surface doping vs. bulk doping of cathode materials for lithium-ion batteries: a review. *Electrochemical Energy Reviews*, *5*(4), p.2.
15. Shannon, R. D. Revised effective ionic radii and systematic studies of interatomic distances in halides and chalcogenides, *Acta Crystallogr., Sect. A: Cryst. Phys., Diffr., Theor. Gen. Crystallogr.*, **1976**, *32*, 751–767. DOI: 10.1107/S0567739476001551.
16. Berdiyrov, G. R. Optical properties of functionalized Ti₃C₂T₂ (T = F, O, OH) MXene: first-principles calculations, *AIP Adv.*, **2016**, *6*(5), 055105. DOI: 10.1063/1.4943752.
17. Blaha, P.; Schwarz, K.; Madsen, G. K. H.; Kvasnicka, D.; Luitz, J. *WIEN2k, An Augmented Plane Wave + Local Orbitals Program for Calculating Crystal Properties*, Technical University of Vienna, Austria, **2001**, pp. 1–302.



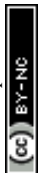
18. Keal, T. W.; Tozer, D. J. A semiempirical generalized gradient approximation exchange–correlation functional, *J. Chem. Phys.*, **2004**, *121*(12), 5654–5660. DOI: 10.1063/1.1778374.
19. Chen, W.; Pöhls, J. H.; Hautier, G.; Broberg, D.; Bajaj, S.; Aydemir, U.; Gibbs, Z. M.; Zhu, H.; Asta, M.; Snyder, G. J.; Meredig, B. Understanding thermoelectric properties from high-throughput calculations: trends, insights, and comparisons with experiment, *J. Mater. Chem. C*, **2016**, *4*(20), 4414–4426. DOI: 10.1039/C5TC04339E.
20. Carrete, J.; Mingo, N.; Wang, S.; Curtarolo, S. Nanograined half-Heusler semiconductors as advanced thermoelectrics: an *ab initio* high-throughput statistical study, *arXiv*, **2014**, arXiv:1408.5859. DOI: 10.48550/arXiv.1408.5859.
21. Miyata, M.; Ozaki, T.; Takeuchi, T.; Nishino, S.; Inukai, M.; Koyano, M. High-throughput screening of sulfide thermoelectric materials using electron transport calculations with OpenMX and BoltzTraP. *J. Electron. Mater.* **2018**, *47*, 3254–3259. DOI: 10.1007/s11664-017-6020-9
22. Shamsieva, A.; Evseev, A.; Kaviani, S.; Nedopekin, O. V.; Zakaryan, H.; Piyanzina, I. DFT analysis of furan-based covalent organic framework as electrode materials for lithium and calcium ion batteries. *Comput. Theor. Chem.*, **2025**, *125*, 115445, DOI: 10.1016/j.comptc.2025.115445.
23. Fatheema, J.; Fatima, M.; Monir, N. B.; Khan, S. A.; Rizwan, S. A comprehensive computational and experimental analysis of stable ferromagnetism in layered 2D Nb-doped Ti₃C₂ MXene, *Physica E*, **2020**, *124*, 114253. DOI: 10.1016/j.physe.2020.114253.
24. Tong, Z.; Suo, Y.; Zhang, S.; Yang, J. Spin-polarized DFT+U study of surface-functionalized Cr₃C₂ MXenes: tunable electronic and magnetic behavior for spintronics, *Mater.*, **2025**, *18*(15), 3709. DOI: 10.3390/ma18153709.
25. Aguilera-Granja, F.; Aguilera-del-Toro, R. H.; Morán-López, J. L. A first-principles systematic study of the structural, electronic, and magnetic properties of Heusler X₂MnZ with X = Fe, Co, Ni, Cu, Ru, Rh, Pd, Ag, Pt, Au and Z = Al, Si, Ga, Ge, In and Sn, *Mater. Res. Express*, **2019**, *6*(10), 106118. DOI: 10.1088/2053-1591/ab243c.
26. Bassman Oftelie, L.; Rajak, P.; Kalia, R. K.; et al. Author Correction: Active learning for accelerated design of layered materials, *npj Comput. Mater.*, **2022**, *8*, 215. DOI: 10.1038/s41524-022-00902-8.
27. Ricci, F.; Chen, W.; Aydemir, U.; Snyder, G. J.; Rignanese, G. M.; Jain, A.; Hautier, G. An *ab initio* electronic transport database for inorganic materials, *Sci. Data*, **2017**, *4*, 170085. DOI: 10.1038/sdata.2017.85.
28. Wang, L.; Liu, W.; Bai, F.; Zheng, X.; Yin, C.; Wei, J.; Ma, J.; Bai, H.; Dong, B. Theoretical study on lithium storage performance of V-doped Ti₂CO₂ MXene, *RSC Adv.*, **2024**, *14*, 19945. DOI: 10.1039/d4ra03618b.
29. Gonzalez, J. W.; Vizcaya, S.; Suarez Morell, E. V2C-based lithium batteries: the influence of magnetic phase and Hubbard interaction, *arXiv*, **2022**, arXiv:2204.04764. DOI: 10.48550/arXiv.2204.04764.
30. Yan, R.-W.; Li, X.-H.; Zhang, R.-Z.; Cui, H.-L. Computational investigation on Cr-doped Sc₂CO₂ MXene under strain for electronic properties, quantum capacitance, and photocatalytic activity, *Langmuir*, **2024**, *40*(37), 19619–19630. DOI: 10.1021/acs.langmuir.4c02282.



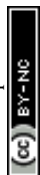
31. Yan, X.; Cao, W.; Li, H. Thermoelectric properties of $X_3N_2O_2$ ($X = \text{Hf, Zr}$) MXene monolayers: a first-principles study. *RSC Adv.*, **2023**, *13*, 18323–18327, DOI: 10.1039/D3RA02835F.
32. Oliveira, F. B.; Lima, E. N.; da Silva, M. C.; da Rosa, A. L.; Frauenheim, T. Exploring charge density distribution and electronic properties of hybrid organic-germanium layers, *Phys. Chem. Chem. Phys.*, **2020**, *22*, 22055–22065. DOI: 10.1039/D0CP03024D.
33. Fatima, M.; Fatheema, J.; Monir, N. B.; Siddique, A. H.; Khan, B.; Islam, A.; Akinwande, D.; Rizwan, S. Nb-doped MXene with enhanced energy storage capacity and stability, *Front. Chem.*, **2020**, *8*, 168. DOI: 10.3389/fchem.2020.00168.
34. Sun, Q.; Fu, Z.; Yang, Z. Tunable magnetic and electronic properties of the Cr-based MXene (Cr_2C) with functional groups and doping, *J. Magn. Magn. Mater.*, **2020**, *514*, 167141. DOI: 10.1016/j.jmmm.2020.167141.
35. Khazaei, M.; Arai, M.; Sasaki, T.; Chung, C.-Y.; Venkataramanan, N. S.; Estili, M.; Sakka, Y.; Kawazoe, Y. Novel electronic and magnetic properties of two-dimensional transition metal carbides and nitrides, *Adv. Funct. Mater.*, **2013**, *23*, 2185–2192. DOI: 10.1002/adfm.201202502.
36. Soundiraraju, B.; George, B. K. Two-dimensional titanium nitride (Ti_2N) MXene: synthesis, characterization, and potential application as surface-enhanced Raman scattering substrate, *ACS Nano*, **2017**, *11*, 8892–8900. DOI: 10.1021/acsnano.7b03129.
37. Anasori, B.; Lukatskaya, M. R.; Gogotsi, Y. 2D metal carbides and nitrides (MXenes) for energy storage, *Nat. Rev. Mater.*, **2017**, *2*, 16098. DOI: 10.1038/natrevmats.2016.98.
38. Ebisawa, F.; Kurokawa, T.; Nara, S. Electrical properties of polyacetylene/polysiloxane interface, *J. Appl. Phys.*, **1983**, *54*, 3255–3259. DOI: 10.1063/1.332488.
39. Shein, I. R.; Ivanovskii, A. L. Planar nano-block structures $\text{Ti}_{n+1}\text{Al}_{0.5}\text{C}_n$ and $\text{Ti}_{n+1}\text{C}_n$ ($n = 1, 2$) from MAX phases: structural, electronic properties and relative stability from first-principles calculations, *Superlattices Microstruct.*, **2012**, *52*(2), 147–157. DOI: 10.1016/j.spmi.2012.04.014.
40. Yaresko, A. N. Electronic band structure and exchange interactions in ferromagnetic CrO_2 , *Phys. Rev. B*, **2008**, *77*, 115106. DOI: 10.1103/PhysRevB.77.115106.
41. Dudarev, S. L.; Botton, G. A.; Savrasov, S. Y.; Humphreys, C. J.; Sutton, A. P. Electron-energy-loss spectra and the structural stability of nickel oxide: an LSDA+U study, *Phys. Rev. B*, **1998**, *57*, 1505–1509. DOI: 10.1103/PhysRevB.57.1505.
42. Chen, Y.; Li, X.; Wang, Z.; Zhou, J.; Sun, Z. Magnetic properties and tunable electronic structures of transition-metal-doped MXenes: a first-principles study, *J. Phys. Chem. C*, **2019**, *123*, 17987–17994. DOI: 10.1021/acs.jpcc.9b03654.
43. Wang, H.; Feng, H.; Li, J.; et al. Graphene and graphene-like anode materials for lithium-ion batteries, *Adv. Mater.*, **2014**, *26*, 4880–4900. DOI: 10.1002/adma.201306031.
44. Snyder, G. J.; Toberer, E. S. Complex thermoelectric materials, *Nat. Mater.*, **2008**, *7*, 105–114. DOI: 10.1038/nmat2090.



45. Xu, B.; Qi, Y.; Liu, C.; et al. Recent progress in MXene-based materials for electrochemical energy storage, *Adv. Funct. Mater.*, **2020**, *30*, 1905812. DOI: 10.1002/adfm.201905812.
46. Beretta, D.; Neophytou, N.; Hodges, J. M.; Kanatzidis, M. G.; Narducci, D.; Martin-Gonzalez, M.; Beekman, M.; Balke, B.; Cerretti, G.; Tremel, W.; Zevalkink, A.; Hofmann, A. I.; Müller, C.; Dörfling, B.; Campoy-Quiles, M.; Caironi, M. Thermoelectrics: from history, a window to the future, *Mater. Sci. Eng., R*, **2019**, *138*, 100501. DOI: 10.1016/j.mser.2018.09.001.
47. Berdiyrov, G. Effect of lithium and sodium ion adsorption on the electronic transport properties of Ti_3C_2 MXene, *Appl. Surf. Sci.*, **2015**, *359*, 161–165. DOI: 10.1016/j.apsusc.2015.10.050.
48. Tarascon, J.-M.; Armand, M. Issues and challenges facing rechargeable lithium batteries, *Nature*, **2001**, *414*, 359–367. DOI: 10.1038/35104644.
49. Hammer, B.; Nørskov, J. K. Theoretical surface science and catalysis—calculations and concepts, *Adv. Catal.*, **2000**, *45*, 71–129. DOI: 10.1016/S0360-0564(02)45013-4.
50. Xia, M.; Zhang, T.; Wu, J.; Lu, W.; Pan, Z.; Qiao, J. Transition metal layer substitution in Mo_2CS_2 MXene: enhanced Li adsorption and electronic structure modulation, *ACS Omega*, **2023**, *8*, 23412–23420. DOI: 10.1021/acsomega.3c02080.
51. Tang, Q.; Zhou, Z.; Shen, P. Are MXenes promising anode materials for Li ion batteries? Computational studies on electronic properties and Li storage capability of Ti_3C_2 and $\text{Ti}_3\text{C}_2\text{X}_2$ (X = F, OH) monolayer, *J. Am. Chem. Soc.*, **2012**, *134*, 16909–16916. DOI: 10.1021/ja308463r.
52. Eames, C.; Islam, M. S. Ion intercalation into two-dimensional transition-metal carbides: global screening for new high-capacity battery materials, *J. Am. Chem. Soc.*, **2014**, *136*, 16270–16276. DOI: 10.1021/ja508154e.
53. Lu, N., Li, L. and Liu, M., **2016**. A review of carrier thermoelectric-transport theory in organic semiconductors. *Physical Chemistry Chemical Physics*, *18*(29), pp.19503-19525.
54. Sun, P., Wei, B., Zhang, J., Tomczak, J.M., Strydom, A.M., Søndergaard, M., Iversen, B.B. and Steglich, F., **2015**. Large Seebeck effect by charge-mobility engineering. *Nature communications*, *6*(1), p.7475.
55. Poncé, S., Li, W., Reichardt, S. and Giustino, F., **2020**. First-principles calculations of charge carrier mobility and conductivity in bulk semiconductors and two-dimensional materials. *Reports on Progress in Physics*, *83*(3), p.036501.
56. Frenking, G. and Fröhlich, N., **2000**. The nature of the bonding in transition-metal compounds. *Chemical reviews*, *100*(2), pp.717-774.
57. Mallick, M.M. and Vitta, S., **2017**. Giant Enhancement in High-Temperature Thermoelectric Figure-of-Merit of Layered Cobalt Oxide, LiCoO_2 , Due to a Dual Strategy □ Co-Substitution and Lithiation. *Inorganic chemistry*, *56*(10), pp.5827-5838.
58. Ohno, Y., Young, D.K., Beschoten, B.A., Matsukura, F., Ohno, H. and Awschalom, D.D., **1999**. Electrical spin injection in a ferromagnetic semiconductor heterostructure. *Nature*, *402*(6763), pp.790-792.



59. Zhu, Y., Gao, T., Fan, X., Han, F. and Wang, C., **2017**. Electrochemical techniques for intercalation electrode materials in rechargeable batteries. *Accounts of chemical research*, *50*(4), pp.1022-1031.
60. Eames, C. and Islam, M.S., **2014**. Ion intercalation into two-dimensional transition-metal carbides: global screening for new high-capacity battery materials. *Journal of the American Chemical Society*, *136*(46), pp.16270-16276.
61. Ju, W., Li, T., Su, X., Li, H., Li, X. and Ma, D., **2017**. Au cluster adsorption on perfect and defective MoS₂ monolayers: structural and electronic properties. *Physical Chemistry Chemical Physics*, *19*(31), pp.20735-20748.
62. Naaz, H.; Malik, F. P.; Mahmood, A.; Irfan, A. Investigation of 2D Nb₃C₂-Based MXenes as the Anode Material for LIBs: A Theoretical Study. *ACS Omega*, 2025, *10*, 5283–5295.
63. Wang, L., Liu, W., Bai, F., Zheng, X., Yin, C., Wei, J., Ma, J., Bai, H. and Dong, B., **2024**. Theoretical study on lithium storage performance of V-doped Ti₂CO₂ MXene. *RSC advances*, *14*(28), pp.19945-19952.
64. Wang, J. and Han, W.Q., **2022**. A review of heteroatom doped materials for advanced lithium-sulfur batteries. *Advanced Functional Materials*, *32*(2), p.2107166.
65. Hiemstra, T. and Van Riemsdijk, W.H., **1996**. A surface structural approach to ion adsorption: the charge distribution (CD) model. *Journal of colloid and interface science*, *179*(2), pp.488-508.
66. Mercer, M.P., Peng, C., Soares, C., Hoster, H.E. and Kramer, D., **2021**. Voltage hysteresis during lithiation/delithiation of graphite associated with meta-stable carbon stackings. *Journal of Materials Chemistry A*, *9*(1), pp.492-504.
67. Yang, C., Yu, S., Ma, Y., Lin, C., Xu, Z., Zhao, H., Wu, S., Zheng, P., Zhu, Z.Z., Li, J. and Wang, N., **2017**. Cr³⁺ and Nb⁵⁺ co-doped Ti₂Nb₁₀O₂₉ materials for high-performance lithium-ion storage. *Journal of power sources*, *360*, pp.470-479.
68. Prenger, K.E., **2022**. *MXenes and Their Heterostructures with Oxides as Electrodes for Supercapacitors* (Doctoral dissertation, Tulane University).
69. Santoy-Flores, R., Fernández-Escamilla, H.N., Páez-Ornelas, J.I., Perez-Tijerina, E.G., Guerrero-Sánchez, J., Ponce-Pérez, R., Takeuchi, N. and Moreno-Armenta, M.G., **2024**. Nb₂C and Nb₂CO₂ MXenes as anodes in Li-ion batteries: a comparative study by first-principles calculations. *ACS omega*, *9*(26), pp.28903-28911.



Data availability Statement:

The computational data that support the findings of this study are available upon request. All the related data is presented in the form of figures and tables in the manuscript.

